Journal of Computational Physics 407 (2020) 109223

Contents lists available at ScienceDirect

Journal of Computational Physics

www.elsevier.com/locate/jcp

Lattice Boltzmann equation with Overset method for moving objects in two-dimensional flows

Pierre Lallemand [a], Li-Shi Luo [a,b,*]

[a] Computational Science Research Center, Beijing 100193, China
[b] Department of Mathematics & Statistics, Old Dominion University, Norfolk, VA 23529, USA

ARTICLE INFO

Article history:
Received 14 November 2018
Received in revised form 21 December 2019
Accepted 28 December 2019
Available online 13 January 2020

Keywords:
Moving boundary problems in Navier-Stokes flows
Lattice Boltzmann equation
Overset method
Rotational frame of reference

ABSTRACT

This work combines the lattice Boltzmann equation (LBE) and the overset method to simulate moving boundary problems in Navier-Stokes flows in two dimensions (2D). The transformation of the velocity moments of the distribution functions between a moving frame of reference and the one at rest is analyzed. The flow past a cylinder moving with a prescribed motion is used to validate the proposed LBE-overset method. We show that the proposed LBE-overset method does reduce the numerical noise generated by the relative motion between a moving object and the underlying Eulerian mesh for flow fields by several orders of magnitude.

1. Introduction

The lattice Boltzmann equation (LBE) [1–3] has been widely applied to simulate the moving boundary problem in fluid dynamics for particulate flows with rigid particles [4–14] or deformable ones [15–19] and fluid-fluid interfacial flows [20–25]. The present work concerns with the moving boundary problem of a rigid body moving in fluid. There are two approaches in the LBE to treat such problem, *i.e.*, the sharp-interface method based on the bounce-back scheme [26,27] and the immersed-boundary method [28,22,29]. The present work concerns the sharp-interface method for the moving boundary of a fluid-solid interface.

In the LBE, the sharp-interface treatment of a fluid-solid interface is similar to the cut-cell method (cf., *e.g.*, [30,31]). The LBE for flow fields is solved on an Eulerian Cartesian mesh, and the numerical boundary of a rigid body in fluid is defined by the intersections of its geometric surface and the grid lines of the underlying Eulerian Cartesian mesh [26]. The boundary of the body moves with respect to the fixed mesh thus the grid points on the Eulerian mesh move in and out of fluid domain through the boundary as the body moves in fluid, and this movement of the body with the fixed mesh generates numerical noises [32].

In this work, we propose to combine the overset or composite-grid technique [33–36] with the LBE to treat the moving boundary problem. As we will demonstrate later, the LB-Overset approach can significantly reduce the numerical noise seen in the LB-sharp-interface approach. The overset method has been adopted in the LBE previously to simulate rotating flows and the term sliding mesh has been used (cf., *e.g.*, [37–39]). The overset approach has two essential ingredients: (a) a composite of the meshes fixed with the local frame of reference which is attached to the bodies moving/rotating with respect to the underlying fixed Eulerian mesh for fluid in the frame of reference at rest, and (b) the communications and

* Corresponding author at: Department of Mathematics & Statistics, Old Dominion University, Norfolk, VA 23529, USA.
E-mail address: lluo@odu.edu (L.-S. Luo).

https://doi.org/10.1016/j.jcp.2019.109223
0021-9991/

matching information between the moving and fixed meshes. With a moving/rotating mesh, the forces due to the change of frame of reference can be directly added to the distributions [37,38] in the LBE or the moments of the distributions [39]. In the work of Li [37] and Zhang et al. [38], the matching between the moving and fixed meshes are achieved by passing only the mass density and momentum density, *i.e.*, the equilibrium information, via some volumetric boundary conditions which amount to some interpolations [40]; while in the work of Far et al. [39], the interpolations are applied to all the moments to ensure that not only the equilibrium information, but also the nonequilibrium one, are passing between to mesh systems with sufficient accuracy.

The key contribution of the present work is the analysis of transformation of the moments between the frames of reference with relative motion based on the theory of rigid-body motion, which has yet to be done within the context of the lattice Boltzmann method, thus the approach proposed in this work differs from the previous ones (cf., *e.g.*, [37–39]). It should be emphasized that only when the theory of transforming moments between different frames of references are fully understood, the numerical treatment of moving/rotating frames in the lattice Boltzmann method is assured to be accurately realized and implemented so to ensure the fidelity of simulations using the lattice Boltzmann method. This issue is particularly acute for simulating of flows with particulate suspensions [5,41,42,8,43,9,44,10,28,45,46,11]. As we will demonstrate later in this work, one immediate benefit of the proposed overset-LBE approach is significant reduction of the noise generated by movements of grid nodes in and out of a fluid domain in simulations of moving object [32].

The remainder of this paper is organized as follows. Section 2 discusses the numerical techniques used in this work, including a brief description of the LBE model with nine discrete velocities in two dimensional (2D) space (the D2Q9 model) and the overset technique in the context of the LBE. The central part of this section is the analysis of transform of the velocity moments of the distribution functions between a frame of reference at rest to a rotational one. Section 3 presents the numerical results of this work. A disc with given linear and rotational velocities in a rectangular domain is used as a test to validate the proposed LB-Overset method. The results show that the proposed method is effective to reduce the numerical noises generated by the relative movement of a rigid body with respect to the underlying fixed Cartesian mesh. Finally, Section 4 concludes the paper.

2. The methodology

We will describe the theory and implementation of the lattice Boltzmann equation with overset meshes in this section. In this work we will restrict ourselves to two dimensions (2D), although the method itself by no means is limited to 2D and it has been implemented in three dimensions (3D). Section 2.1 provides a brief description of the lattice Boltzmann model with nine discrete velocities in 2D (D2Q9 model), the collision is based on the multiple-relaxation-time model which is carried out in moment space. Section 2.2 about the overset approach in the setting of the LBE is the theoretical core of this work, which includes three parts. The first part is the data passing between a moving mesh and a fixed one in Sec. 2.2.1. The second part concerns about the transformation of moments in a moving frame of reference. The third and last part is about forces induced by a rotating frame of reference in Sec. 2.2.3.

2.1. The lattice Boltzmann equation

We will use the lattice Boltzmann equation with the multiple-relaxation-time (MRT) collision model [47–49]. An LBE model of q discrete velocities, $\{\boldsymbol{\xi}_i | i = 0, 1, \ldots, q-1\}$, in d dimensions is denoted as DdQq model. In general, the lattice Boltzmann equation on a lattice $\delta_x \mathbb{Z}^d$ of the lattice spacing δ_x and with discrete time $\{t_n | n \in \mathbb{N}_0\}$ can be written concisely in vector notation as the following:

$$\mathbf{f}(\boldsymbol{r}_j + \delta_t \boldsymbol{\xi},\, t_n + \delta_t) = \mathbf{f}(\boldsymbol{r}_j,\, t_n) - \mathbf{M} \cdot \mathbf{S} \cdot \Big[\mathbf{m}(\boldsymbol{r}_j,\, t_n) - \mathbf{m}^{(0)}(\boldsymbol{r}_j,\, t_n) \Big], \tag{1}$$

where up-right bold face symbols denote q-dimensional vectors in $\mathbb{R}^q$:

$$\begin{aligned}
&\mathbf{f}(\boldsymbol{r}_j + \delta_t \boldsymbol{\xi},\, t_n + \delta_t) := (f_0(\boldsymbol{r}_j,\, t_n + \delta_t),\, f_1(\boldsymbol{r}_j + \delta_t \boldsymbol{\xi}_1,\, t_n + \delta_t),\, \ldots,\, f_{q-1}(\boldsymbol{r}_j + \delta_t \boldsymbol{\xi}_{q-1},\, t_n + \delta_t))^\dagger, \\
&\mathbf{f}(\boldsymbol{r}_j,\, t_n) := (f_0(\boldsymbol{r}_j,\, t_n),\, f_1(\boldsymbol{r}_j,\, t_n),\, \ldots,\, f_{q-1}(\boldsymbol{r}_j,\, t_n))^\dagger, \\
&\mathbf{m}(\boldsymbol{r}_j,\, t_n) := (m_0(\boldsymbol{r}_j,\, t_n),\, m_1(\boldsymbol{r}_j,\, t_n),\, \ldots,\, m_{q-1}(\boldsymbol{r}_j,\, t_n))^\dagger, \\
&\mathbf{m}^{(0)}(\boldsymbol{r}_j,\, t_n) := (m_0^{(0)}(\boldsymbol{r}_j,\, t_n),\, m_1^{(0)}(\boldsymbol{r}_j,\, t_n),\, \ldots,\, m_{q-1}^{(0)}(\boldsymbol{r}_j,\, t_n))^\dagger,
\end{aligned}$$

$\mathbf{f}(\boldsymbol{r}_j,\, t_n)$, $\mathbf{m}(\boldsymbol{r}_j,\, t_n)$, and $\mathbf{m}^{(0)}(\boldsymbol{r}_j,\, t_n)$ denote the vectors of the distribution functions, the moments, and the equilibrium moments (which are functions of the conserved quantities and will be specified later), respectively; $\mathbf{f}(\boldsymbol{r}_j + \delta_t \boldsymbol{\xi},\, t_n + \delta_t)$ serves as a convenient notation which includes the distributions not at the same location, but about other lattice nodes $\{\boldsymbol{r}_j + \delta_t \boldsymbol{\xi}_i | i = 0, 1, \ldots, (q-1)\}$ about the node $\boldsymbol{r}_j$; $\dagger$ denotes transpose operator, $\mathbf{M}$ is the $q \times q$ projection matrix mapping the distribution functions $\{f_i\}$ to their velocity moments $\{m_i\}$:

$$\mathbf{m} = \mathbf{M} \cdot \mathbf{f}, \qquad \mathbf{f} = \mathbf{M}^{-1} \cdot \mathbf{m}, \tag{2}$$

and $\mathbf{S}$ is the diagonal relaxation matrix whose diagonal elements are the relaxation rates which determine the dissipation of the moments leading to the transport coefficients.

To be concrete, we will use the D2Q9 model in what follows. The discrete velocities are: $\boldsymbol{\xi}_0 = (0, 0)c$, $\boldsymbol{\xi}_{1,3} = (\pm 1, 0)c$, $\boldsymbol{\xi}_{2,4} = (0, \pm 1)c$, and $\boldsymbol{\xi}_{5,6,7,8} = (\pm 1, \pm 1)c$, where $c := \delta_x/\delta_t$. The ordering of the moments are

$$\mathbf{m} := (\rho,\ j_x,\ j_y,\ e,\ p_{xx},\ p_{xy},\ q_x,\ q_y,\ \epsilon)^\dagger, \tag{3}$$

where $\boldsymbol{j} := (j_x,\ j_y) = \rho(u_x,\ u_y)$ is the momentum. With this ordering of moments (properly orthogonalized) and adequate normalization, the projection matrix is

$$\mathbf{M} = \begin{pmatrix} 1 & 1 & 1 & 1 & 1 & 1 & 1 & 1 & 1 \\ 0 & 1 & 0 & -1 & 0 & 1 & -1 & -1 & 1 \\ 0 & 0 & 1 & 0 & -1 & 1 & 1 & -1 & 1 \\ -4 & -1 & -1 & -1 & -1 & 2 & 2 & 2 & 2 \\ 0 & 1 & -1 & 1 & -1 & 0 & 0 & 0 & 0 \\ 0 & 0 & 0 & 0 & 0 & 1 & -1 & 1 & -1 \\ 0 & -2 & 0 & 2 & 0 & 1 & -1 & -1 & 1 \\ 0 & 0 & -2 & 0 & 2 & 1 & 1 & -1 & -1 \\ 4 & -2 & -2 & -2 & -2 & 1 & 1 & 1 & 1 \end{pmatrix}. \tag{4}$$

The labeling of the discrete velocities $\{\boldsymbol{\xi}_i\}$ is uniquely specified by the second and third rows of $\mathbf{M}$, the elements of which are the x and y components of $\{\boldsymbol{\xi}_i\}$, respectively. The relaxation matrix is given by:

$$\mathbf{S} = \mathrm{diag}(1,\ 1,\ 1,\ s_e,\ s_\nu,\ s_\nu,\ s_q,\ s_q,\ s_\epsilon). \tag{5}$$

For the model considered here, the only conserved quantities are the mass density ρ and the flow momentum $\boldsymbol{j} := \rho\boldsymbol{u} := (j_x,\ j_y) := \rho(u_x,\ u_y)$. The equilibria of conserved moments, *i.e.*, ρ, j_x and j_y, are themselves, and the equilibria of non-conserved moments are given by

$$e^{(0)} = -2\rho + \frac{3}{\rho}(j_x^2 + j_y^2), \tag{6a}$$

$$p_{xx}^{(0)} = \frac{1}{\rho}(j_x^2 - j_y^2), \quad p_{xy}^{(0)} = \frac{1}{\rho} j_x j_y, \tag{6b}$$

$$q_{x,y}^{(0)} = -j_{x,y}, \tag{6c}$$

$$\epsilon^{(0)} = \rho - \frac{3}{\rho}(j_x^2 + j_y^2). \tag{6d}$$

In the equilibria of $q_{x,y}$, terms of the form $j_{x,y}^3$ are not considered, even though they are necessary to eliminate the numerical artifacts on the Galilean invariance of the LBE due to the terms of $|\boldsymbol{u}|^3$, which also appears in the form of the velocity-dependence of the viscosity. To eliminate this cubic-term artifact on the Galilean invariance (cf., *e.g.*, [50]), it requires at least thirteen velocities — the D2Q9 model does not possess sufficient degrees of freedom for this purpose. Therefore, the cubic terms in the equilibria are not considered in the D2Q9 model.

With the equilibria given by Eqs. (6), the speed of sound is

$$c_s = \frac{1}{\sqrt{3}} c, \tag{7}$$

and the kinematic shear viscosity ν and the kinematic bulk viscosity ζ are given by

$$\nu = \frac{1}{3}\left(\frac{1}{s_\nu} - \frac{1}{2}\right) c\delta_x, \qquad \zeta = \frac{1}{3}\left(\frac{1}{s_e} - \frac{1}{2}\right) c\delta_x. \tag{8}$$

2.2. LB-Overset method for moving boundary

There are two types of meshes in the LB-overset method. The first is a mesh "F" covering the entire flow domain Ω which is the frame of reference at rest. The second one is a mesh "G" that carries a rigid body fixed with it and is moving with respect to mesh F. The success of the overset method critically depends on the accuracy of data communication between these two meshes, F and G. In what follows, for the sake of simplicity we will assume that both meshes, F and G, are square Cartesian meshes with an equal grid spacings δ_x. In general, the grid spacings in two meshes can be different, and the same can be said for the time step size δ_t.

The LBE consists of two essential steps: collision and advection. Since the discrete velocity sets on both F and G meshes are identical, the advections on both F and G are identical, too, thus need not to be elaborated. In order to carry out the

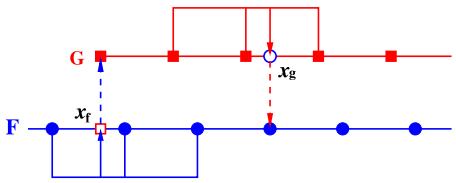

Fig. 1. ID illustration of interpolations between two meshes F (fixed) and G (moving). Solid discs and squares are the grid points on mesh F and G, respectively. The unfilled circle (unfilled square) is the location on G (F) where the data are transferred to a grid node on the mesh F (G), as indicated by arrows of dashed lines. The data on these locations are obtained by interpolations indicated in the text.

collision process in both meshes F and G, exchange of data between two meshes are required. We shall decompose the collision process into several steps. First, we must consider the data exchange between two meshes in a static situation because the grids of two meshes do not coincide in general. Second, we must consider the transformation of data between two different frames of reference. And third, we must consider additional forces due to the relative motion between two meshes. After these three steps, the relaxation process can be carried out. We shall discuss all these steps in detail.

2.2.1. Data passing between two meshes with relative motion

Usually the mesh points of F and G do not coincide with each other. Thus the first step is to interpolate data on one mesh to the locations which coincide with grid nodes on the other mesh so the data can be passed from the former mesh to the latter one. It is assumed the entire domain covered by the moving mesh G is in the interior of the domain covered by the fixed mesh F. The data passing from the fixed mesh F to the moving mesh G takes place at the boundary nodes of G, ∂G, while the data passing from the moving mesh G to the fixed mesh F takes place at a subset of interior nodes of G, which will be explained later.

Fig. 1 illustrates a one-dimensional situation. To transfer data from the fixed mesh F to the moving mesh G, the data have to be interpolated to an off-grid location on F, marked as $\boldsymbol{x}_{\rm f}$, which coincides with a boundary node on G; similarly, to transfer data from the moving mesh G to the fixed mesh F, the data have to be interpolated to an off-grid location on G, marked as $\boldsymbol{x}_{\rm g}$, which coincides with a node on F. The off-grid information, *i.e.*, the locations indicated by open square ($\square$) on fixed mesh F or open circle ($\bigcirc$) on moving mesh G (cf. Fig. 1), is obtained by interpolations, which are to be discussed next.

We emphasize that the data to be passed between two meshes should be the moments $\{m_i\}$ and $\{n_i\}$, but not the distribution functions $\{f_i\}$ and $\{g_i\}$, because the moments have physical significance and tensorial properties which must be preserved in the transformation from one frame of reference to another. Thus the data transformation between meshes is carried out in moment space, so are the interpolations. If instead the distribution functions are used in the data transfer between different frames of reference, the tensorial properties of the moments may not be preserved. To be consistent with the second order accuracy of the LBE model, it is sufficient to perform second-order interpolations for the conserved moments, *i.e.*, ρ, j_x and j_y (or ϱ, J_x and J_y) and bi-linear interpolations for the remaining six non-conserved moments.

The second-order interpolation for a function $\phi(\boldsymbol{r})$ on 2D plane $\boldsymbol{r}\in\mathbb{R}^2$ is given by the following:

$$\phi(\boldsymbol{r}_j+\boldsymbol{r})=\frac{1}{8}\sum_{i=0}^{8}W_i(x,\,y)\phi(\boldsymbol{r}_j+\delta_t\boldsymbol{\xi}_i), \tag{9}$$

where $\boldsymbol{r}:=(x,\,y)$ is the position with respect to the lattice node $\boldsymbol{r}_j$ where interpolated information is needed (cf. Fig. 2), and $\{W_i(x,\,y)|i=0,\,1,\,\ldots,\,8\}$ are the weights of the interpolation given by:

$$W_0(x,\,y):=4[1-(x^2+y^2)][2-(x^2+y^2)], \tag{10a}$$
$$W_1(x,\,y):=2(1-y^2)y^2+2\{4+[3-(2+x)x-2y^2]x-2y^2\}x, \tag{10b}$$
$$W_2(x,\,y):=2(1-x^2)x^2+2\{4+[3-(2+y)y-2x^2]y-2x^2\}y, \tag{10c}$$
$$W_3(x,\,y):=2(1-y^2)y^2-2\{4-[3+(2-x)x-2y^2]x-2y^2\}x, \tag{10d}$$
$$W_4(x,\,y):=2(1-x^2)x^2-2\{4-[3+(2-y)y-2x^2]y-2x^2\}y, \tag{10e}$$
$$W_5(x,\,y):=-[2-(1+x)x-(1+y)y][(1+x)x+(1+y)y], \tag{10f}$$
$$W_6(x,\,y):=[2+(1-x)x-(1+y)y][(1-x)x-(1+y)y], \tag{10g}$$
$$W_7(x,\,y):=[2+(1-x)x+(1-y)y][(1-x)x+(1-y)y], \tag{10h}$$
$$W_8(x,\,y):=-[2-(1+x)x+(1-y)y][(1+x)x-(1-y)y], \tag{10i}$$

and they satisfy the normalization condition $(1/8)\sum_i W_i(x,\,y)=1$. We note that in the LBE setting, $-1<x,\,y<+1$ in (10). The stencil for the 2D interpolation is illustrated in Fig. 2. With the same nine-points stencil one can also construct a bi-quadratic interpolation.

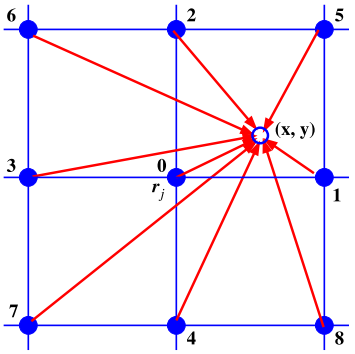

Fig. 2. The nine-points interpolation stencil for computing the information on an off-lattice location, marked by an open circle ◯. The solid discs mark the locations where the data are used in interpolation to obtain the data at the location marked by ◯. The coordinates (x, y) are with respect to the origin set at the lattice node $\boldsymbol{r}_j$ marked with 0.

The bi-linear interpolation used to compute the non-conserved moments at an off-lattice position (x, y) involves only four nearest lattice points surrounding (x, y). An arbitrary point (x, y) with $-1 < x, y < 1$ may fall in one of four quadrants of the 2×2 square (cf. Fig. 2), thus there always exist four points defining a unit square, a quadrant, in which the point (x, y) locates, as illustrated in Fig. 2. Suppose the coordinate (x, y) is in the first quadrant, *i.e.*, $0 < x, y < 1$, then the bi-linear interpolation for a function $\phi(x, y)$ is given by:

$$\phi(\boldsymbol{r}_j + \boldsymbol{r}) = (1-x)(1-y)\phi(\boldsymbol{r}_j) + x(1-y)\phi(\boldsymbol{r}_j + \delta_t\boldsymbol{\xi}_1) + (1-x)y\phi(\boldsymbol{r}_j + \delta_t\boldsymbol{\xi}_2) + xy\phi(\boldsymbol{r}_j + \delta_t\boldsymbol{\xi}_5). \tag{11}$$

We should mention that the bi-linear interpolation (11) uses the stencil identical to the compact interpolation based on the Taylor expansions of the distribution functions proposed by Far et al. [39] which seems to be able to deliver the desirable accuracy [39]. The four-points compact interpolation proposed by Far et al. [39] may require less computation than the interpolation with a nine-points stencil, especially when extending the present work in 3D, which may need a stencil of up to 27 points.

The boundary ∂G of the moving mesh G is defined by a set of grid points on G, which are the point to receive data from the fixed mesh F. A body B moving with respect to the fixing mesh F is covered by the mesh G, and the mesh G should be large enough so that there is a buffer zone between the boundary of the moving body B, ∂B, and the boundary of mesh G moving with the body B, ∂G. The width of this buffer zone should at the least be two grid spacings, so that the interpolations required for passing data from the moving mesh G to the fixed mesh F can be realized.

To ease the implementation, the boundary of G should be simple, either a rectangle or a polygon, while the boundary or the shape of the moving body B can be rather complicated. Because of the simplicity of the boundary of moving mesh G, data passing along its boundary ∂G can be realized in a straightforward manner. This thus avoids the difficulty to deal with the data passing along a complicated moving body. Note however that the list of transfer nodes has to be large enough to fully define the state of F or G on the boundaries.

2.2.2. Transformation of moments on a moving mesh

The data on meshes F and G are two sets of distribution functions, **f** and **g**, respectively, and the corresponding moments **m** and **n**. The moments on the moving mesh G are denoted by:

$$\mathbf{n} = (\varrho,\ J_x,\ J_y,\ E,\ P_{xx},\ P_{xy},\ Q_x,\ Q_y,\ \varepsilon)^{\dagger}. \tag{12}$$

We will consider a rigid body B, which may have a very complicated geometry, fixed on mesh G, which has a regular and simple boundary geometry. Therefore, the problem of a moving complicated rigid body is simplified to the problem of a moving mesh of simply regular boundary. In this setting, the crucial issue to be considered is the coupling between two meshes: the moving mesh G and the mesh at rest F. The transformation of data depends on the state of motion of mesh G and the tensorial properties of the moments, *i.e.*, ρ, e and ϵ are scalars so they are transformed as such, (j_x, j_y) and (q_x, q_y) are vectors, and p_{xx} and p_{xy} are components of a second rank tensor.

The motion of the moving mesh G is determined by its linear velocity $\boldsymbol{V} = (V_x, V_y)$ and its angular velocity ω with respect to a fixed point in space. Denote θ as the angle between the X axis on the moving mesh G and the x axis on the fixed mesh F. Since we do not consider the relativistic effect, the mass density ρ is not affected by the relative motion between the two meshes. Obviously, the momentum on the mesh G is given by:

$$J_x = j_x\cos\theta + j_y\sin\theta + \rho V_x, \qquad J_y = -j_x\sin\theta + j_y\cos\theta + \rho V_y. \tag{13}$$

The 2D rotational operator $\mathbf{R}(\theta)$ in the frame of reference at the rest, which is fixed with the mesh F, and its inverse $\mathbf{R}^{-1}(\theta) = \mathbf{R}(-\theta)$ are given by

$$\mathbf{R}(\theta) := \begin{pmatrix} \cos\theta & \sin\theta \\ -\sin\theta & \cos\theta \end{pmatrix}, \quad \mathbf{R}^{-1}(\theta) := \begin{pmatrix} \cos\theta & -\sin\theta \\ \sin\theta & \cos\theta \end{pmatrix},$$

then Eqs. (13) can be concisely written as the following:

$$\boldsymbol{J} = \mathbf{R}(\theta)\cdot\boldsymbol{j} + \rho\boldsymbol{V}, \quad \boldsymbol{j} = \mathbf{R}(-\theta)\cdot(\boldsymbol{J} - \rho\boldsymbol{V}). \tag{14}$$

The non-conserved moments on the moving mesh G are split into two parts: zeroth- and first-order terms according to the Chapman-Enskog analysis and are given in terms of the moments on F:

$$E = -2\varrho + \frac{3}{\varrho}(J_x^2 + J_y^2) + \delta e = E^{(0)} + \delta e, \tag{15a}$$

$$\begin{aligned} P_{xx} &= \frac{1}{\varrho}(J_x^2 - J_y^2) + \delta p_{xx}\cos 2\theta + \delta p_{xy}\, 2\sin 2\theta \\ &= P_{xx}^{(0)} + \delta p_{xx}\cos 2\theta + \delta p_{xy}\, 2\sin 2\theta, \end{aligned} \tag{15b}$$

$$\begin{aligned} P_{xy} &= \frac{1}{\varrho}J_x J_y - \delta p_{xx}\frac{1}{2}\sin 2\theta + \delta p_{xy}\cos 2\theta \\ &= P_{xy}^{(0)} - \delta p_{xx}\frac{1}{2}\sin 2\theta + \delta p_{xy}\cos 2\theta, \end{aligned} \tag{15c}$$

$$Q_x = -J_x + \delta q_x\cos\theta + \delta q_y\sin\theta = Q_x^{(0)} + \delta q_x\cos\theta + \delta q_y\sin\theta, \tag{15d}$$

$$Q_y = -J_y - \delta q_x\sin\theta + \delta q_y\cos\theta = Q_y^{(0)} - \delta q_x\sin\theta + \delta q_y\cos\theta, \tag{15e}$$

$$\varepsilon = \varrho - \frac{3}{\varrho}(J_x^2 + J_y^2) + \delta\epsilon = \varepsilon^{(0)} + \delta\epsilon, \tag{15f}$$

where δe, δp_{xx}, δp_{xy}, $\delta q_{x,y}$ and $\delta\epsilon$ are the first-order parts of the non-conserved moments on the fixed mesh F:

$$\delta e = e - e^{(0)} = e + 2\rho - \frac{3}{\rho}(j_x^2 + j_y^2), \tag{16a}$$

$$\delta p_{xx} = p_{xx} - p_{xx}^{(0)} = p_{xx} - \frac{1}{\rho}(j_x^2 - j_y^2), \tag{16b}$$

$$\delta p_{xy} = p_{xy} - p_{xy}^{(0)} = p_{xy} - \frac{1}{\rho}j_x j_y, \tag{16c}$$

$$\delta q_{x,y} = q_{x,y} - q_{x,y}^{(0)} = q_{x,y} + j_{x,y}, \tag{16d}$$

$$\delta\epsilon = \epsilon - \epsilon^{(0)} = \epsilon - \rho + \frac{3}{\rho}(j_x^2 + j_y^2). \tag{16e}$$

The above equilibria of the non-conserved moments define their transformation from one mesh to the other. In particular, the formulas for the stresses, P_{xx} and P_{xy}, and the energy flux $\boldsymbol{Q} = (Q_x,\ Q_y)^\dagger$ are re-written as the following:

$$\begin{pmatrix} P_{xx} \\ P_{xy} \end{pmatrix} = \begin{pmatrix} P_{xx}^{(0)} \\ P_{xy}^{(0)} \end{pmatrix} + \begin{pmatrix} \cos 2\theta & 2\sin 2\theta \\ -\frac{1}{2}\sin 2\theta & \cos 2\theta \end{pmatrix} \cdot \begin{pmatrix} \delta p_{xx} \\ \delta p_{xy} \end{pmatrix}, \tag{17a}$$

$$\boldsymbol{Q} = \boldsymbol{Q}^{(0)} + \mathbf{R}\cdot\delta\boldsymbol{q}. \tag{17b}$$

The above formulas clearly indicate that P_{xx} and P_{xy} obey the transformation of components of a second-rank tensor, while $\boldsymbol{Q}$ obeys the transformation of a vector.

It is interesting to note that, without the constant factors 2 and 1/2 in its off-diagonal elements, the transformation matrix for δp_{xx} and δp_{xy} is in fact equal to $\mathbf{R}(2\theta) = \mathbf{R}^2(\theta)$, indicating that the pair $(\delta p_{xx},\ \delta p_{xy})$ does behave like the components of a second-rank tensor, such as $\boldsymbol{uu}$. The factors 2 and 1/2 are due to choices of the equilibria (6) or their normalizations, *i.e.*, the row vectors in $\mathbf{M}$ are not normalized.

2.2.3. Forces on a moving mesh

Because mesh G has a relative motion with respect to mesh F which is fixed to the frame of reference at rest, G is subject to some forces due to the relative motion, including linear accelerating force $\varrho\dot{\boldsymbol{V}}$, centripetal force $\varrho\omega^2\boldsymbol{r}$, Coriolis force $-2\varrho\boldsymbol{\omega}\times\boldsymbol{V}$, and Poincaré force $\varrho\dot{\boldsymbol{\omega}}\times\boldsymbol{r}$, where the vector $\boldsymbol{r}$ is originated at the center of rotation on G. Thus the total force on F and G are:

$$\boldsymbol{F} = \rho \boldsymbol{a} = \varrho \boldsymbol{g}, \tag{18a}$$

$$\boldsymbol{G} = \varrho \boldsymbol{A} = \varrho \left(\boldsymbol{g} + \dot{\boldsymbol{V}} + \omega^2 \boldsymbol{r} - 2\boldsymbol{\omega} \times \boldsymbol{V} + \dot{\boldsymbol{\omega}} \times \boldsymbol{r} \right), \tag{18b}$$

where $\varrho \boldsymbol{g}$ is a body force (for instance due to gravity).

The computational procedure for the LBE+Overset scheme can be summarized as the following. At the time $t = t_n$:

1. Compute moments on both meshes:

$$\mathbf{m} = \mathbf{M} \cdot \mathbf{f}(t_n) \qquad \text{on the fixed mesh F,}$$
$$\mathbf{n} = \mathbf{M} \cdot \mathbf{g}(t_n) \qquad \text{on the moving mesh G;}$$

2. Interpolate moments on both F and G on locations where data passing are required (cf. Fig. 1);
3. Transform moments between mesh F and mesh G according to Eqs. (15);
4. Compute Forces on both mesh F and mesh G according to Eqs. (18);
5. Add one half of the total force to the momentum:

$$\boldsymbol{j}^* = \boldsymbol{j} + \boldsymbol{F}/2 \qquad \text{on the fixed mesh F,}$$
$$\boldsymbol{J}^* = \boldsymbol{J} + \boldsymbol{G}/2 \qquad \text{on the moving mesh G,}$$

   where $\boldsymbol{j}^*$ and/or $\boldsymbol{J}^*$ are the resulting values of the corresponding flow fields at the time t_n (cf., *e.g.*, [51,52]);
6. Use $\boldsymbol{j}^*$ and $\boldsymbol{J}^*$ to compute the equilibria according to Eqs. (6) on both meshes F and G, respectively, then compute the post-collision moments:

$$\mathbf{m}^* = \mathbf{m} - \mathbf{S} \cdot [\mathbf{m} - \mathbf{m}^{(0)}], \qquad \text{on the fixed mesh F,}$$
$$\mathbf{n}^* = \mathbf{n} - \mathbf{S} \cdot [\mathbf{n} - \mathbf{n}^{(0)}], \qquad \text{on the moving mesh G;}$$

7. Add another half of forces to the momentum:

$$\boldsymbol{j}^{**} = \boldsymbol{j}^* + \boldsymbol{F}/2 \qquad \text{on the fixed mesh F,}$$
$$\boldsymbol{J}^{**} = \boldsymbol{J}^* + \boldsymbol{G}/2 \qquad \text{on the moving mesh G;}$$

8. Map moments to distributions on both F and G using $\boldsymbol{j}^{**}$ and $\boldsymbol{J}^{**}$:

$$\mathbf{f} = \mathbf{M}^{-1} \cdot \mathbf{m}(\boldsymbol{j}^{**}) \qquad \text{on the fixed mesh F,}$$
$$\mathbf{g} = \mathbf{M}^{-1} \cdot \mathbf{n}(\boldsymbol{J}^{**}) \qquad \text{on the moving mesh G;}$$

9. Carry out advections on both F and G to obtain $\mathbf{f}(t_{n+1})$ and $\mathbf{g}(t_{n+1})$;
10. Return to Step 1.

3. Numerical results

3.1. Flow configuration and implementation

To test the effectiveness of the proposed scheme for moving boundary problem, we design the following flow consisting of a rotating disc moving in a bounded domain Ω of size $L \times H$. The disc is subject to both a linear and a rotational motion. Its center moves horizontally with a prescribed velocity $\boldsymbol{U} = (U_x(t), 0)$, where

$$U_x(t) = \begin{cases} \dfrac{t_n}{T_0} U_0, & 0 \le t_n \le T_0, \\ U_0, & t_n > T_0. \end{cases} \tag{19}$$

$T_0 = 2000\delta_t$, and $U_0 = 0.05c$, that is, the disc accelerates with a constant acceleration along the horizontal direction, then moves with the constant velocity attained during the acceleration phase. Simultaneously, the cylinder also rotates with a constant angular velocity $\omega_0 = 0.001/\delta_t$ about its center as seen from a fixed reference frame.

The flow domain Ω of size $L \times H$ is covered by a mesh "F" of size $N_x \times N_y$. We choose $L/H = 4$, so $N_x/N_y = 4$. We will use $N_x = 2048$ and $N_y = 512$. The boundary conditions for the vertical boundaries at $x = 0$ and $x = L$ are "free-flow" (or fully developed) boundary conditions. For the horizontal boundaries at $y = 0$ and $y = H$, the periodic boundary conditions are applied. The four corner points of the mesh belong to the vertical boundaries. These boundary conditions are realized as follows:

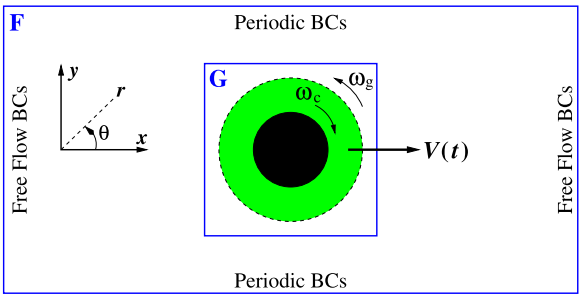

Fig. 3. A schematic of flow configuration and meshes F and G.

$$\mathbf{f}(i_x,\,1) = \mathbf{f}(i_x,\,N_y) \qquad \forall\, \boldsymbol{\xi}_k \cdot \hat{\boldsymbol{y}} > 0,\; 2 \le i_x \le N_x - 1, \tag{20a}$$

$$\mathbf{f}(i_x,\,N_y) = \mathbf{f}(i_x,\,1) \qquad \forall\, \boldsymbol{\xi}_k \cdot \hat{\boldsymbol{y}} < 0,\; 2 \le i_x \le N_x - 1, \tag{20b}$$

$$\mathbf{f}(1,\,i_y) = \mathbf{f}(2,\,i_y), \qquad \forall\, \boldsymbol{\xi}_k \cdot \hat{\boldsymbol{x}} < 0,\; 1 \le i_y \le N_y, \tag{20c}$$

$$\mathbf{f}(N_x,\,i_y) = \mathbf{f}(N_x - 1,\,i_y), \qquad \forall\, \boldsymbol{\xi}_k \cdot \hat{\boldsymbol{x}} > 0,\; 1 \le i_y \le N_y. \tag{20d}$$

Within the flow domain, a sub-domain Ω_{G} is covered by a mesh "G" of size 63×63. A solid disc of radius of $R = 15.8\delta_x$ sits at the center of mesh G.

The communication between the two meshes G and F is carried out at the nodes on G within the ring concentric to the cylinder and with the inner and outer radius of $21.6\delta_x$ and $24.6\delta_x$, respectively. Fig. 3 illustrates the flow domain and meshes.

The Dirichlet boundary conditions at the boundary ∂B of the rigid body B on mesh G are realized as follows. The boundary ∂B intersects with a group of links between two adjacent nodes on mesh G. The locations of the intersects define the boundary ∂B on mesh G. Because the rigid body B does not move on mesh G, its boundary ∂B is fixed with respect to G, so are the intersections and the fluid nodes whose link or links intersect with ∂B. These nodes are the boundary nodes, and the set of them is denoted by:

$$\mathbb{B} := \{\boldsymbol{r}_j,\, \boldsymbol{\xi}_k | \boldsymbol{r}_j \in \Omega\backslash\Omega_{\mathrm{C}};\; \exists\, \boldsymbol{\xi}_k,\, \boldsymbol{r}_j + \delta_t \boldsymbol{\xi}_k \notin \Omega\backslash\Omega_{\mathrm{C}}\}, \tag{21}$$

where Ω_{C} is the domain occupied by the disc or other solid object moving in a flow. The information about the set $\mathbb{B}$, including the positions of the intersects and the boundary nodes, is obtained in the pre-processing stage, and needs to be done only once. It should also be noted that this scheme is independent of the geometric complexity of the boundary ∂B, thus can be implemented for arbitrary complicated geometries, provided that the mesh resolution is sufficient to maintain the geometric accuracy.

With the velocity $\boldsymbol{u}_{\mathrm{B}}$ at the boundary ∂B given, the Dirichlet boundary conditions on mesh G are realized through the linearly interpolated bounce-back scheme at the boundary nodes in $\mathbb{B}$ [26]. In particular, when the rigid body B rotates about its center of mass with an angular velocity $\boldsymbol{\omega}_{\mathrm{C}}$, then the linear velocity at a point $\boldsymbol{x}_{\mathrm{B}}$ on its boundary ∂B is $\boldsymbol{u}_{\mathrm{B}}(\boldsymbol{x}_{\mathrm{B}}) = \boldsymbol{\omega}_{\mathrm{C}} \times \boldsymbol{r}$, where $\boldsymbol{r}$ is the vector from the disc center to the point $\boldsymbol{x}_{\mathrm{B}}$.

The initial position of the disc center is $(x_0,\, y_0) = (L/4,\, H/2)$, *i.e.*, the center of the disc is set at the center line of the flow domain and one-fourth of the domain length from the left initially. The initial conditions for the distribution functions $\{f_i\}$ are of a quiescent one. The mean density is $\rho_0 = 1$, the fluctuating part of the density is $\delta\rho = 0$, and the velocity is $\boldsymbol{u}_0 = \boldsymbol{0}$ throughout the entire flow domain. The distribution functions are set to be the equilibrium distributions with the initial values ρ_0 and $\boldsymbol{u}_0$.

The initial conditions on mesh G are that the density is uniform as on mesh F and the velocity is equal to that of a rigid body rotating about the center of the disc with the angular velocity $-\omega_{\mathrm{G}}$, so the absolute velocity field with respect to mesh F is zero initially.

The Reynolds number of the flow is based on the diameter of the cylinder $D = 2R = 31.6\delta_x$, and speed U_0 *i.e.*,

$$\mathrm{Re} := \frac{U_0 D}{\nu}. \tag{22}$$

The relaxation rate s_ν for the second-order moments related to the stresses is to be determined by the Reynolds number in the simulations. Other relaxation rates, which are not critical to the results of the simulation, include: $s_e = 1.4$, $s_\epsilon = 1.3$, and $s_q = 1.5$ for the second-order moment e, the fourth-order moment ϵ, and the third-order moments $(q_x,\, q_y)$, respectively.

3.2. Hydrodynamic forces

During an LB simulation, the distribution functions $\mathbf{g}$ on the boundary nodes in the set $\mathbb{B}$ on mesh G are used to compute the momentum exchange between fluid and the disc occurring at the boundary ∂B (cf., *e.g.*, [26,53]):

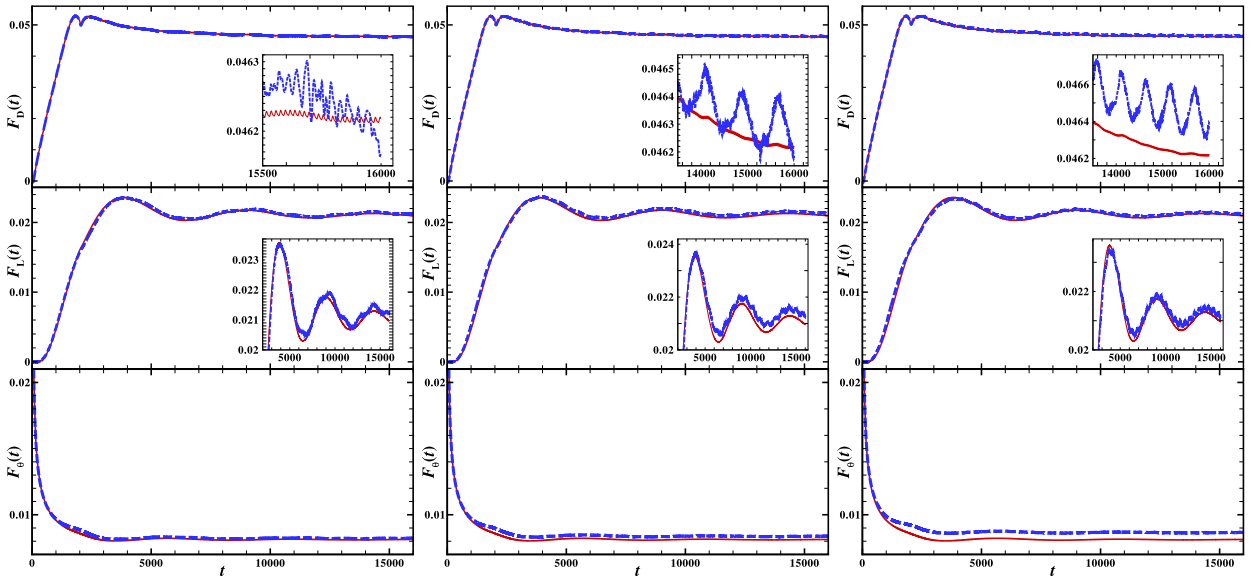

Fig. 4. Re = 30.0. From top to bottom: the evolution of the normalized drag, lift, and tangential forces, $\bar{F}_{\rm D}(t)$, $\bar{F}_{\rm L}(t)$, and $\bar{F}_{\theta}(t)$. From left to right: Case (2) $\omega_{\rm G} = 0.001/\delta_t$ and $\omega_{\rm C} = 0$ (dashed lines) *vs.* Case (1) $\omega_{\rm G} = 0$ and $\omega_{\rm C} = 0.001/\delta_t$ (solid lines); Case (3) $\omega_{\rm G} = 0.002/\delta_t$ and $\omega_{\rm C} = -0.001/\delta_t$ (dashed lines) *vs.* Case (1) (solid lines); and Case (4) $\omega_{\rm G} = 0.003/\delta_t$ and $\omega_{\rm C} = -0.002/\delta_t$ (dashed lines) *vs.* Case (1) (solid lines). The inserts in the top row amplify the numerical artifacts of frequencies $2\omega_{\rm G}/\pi$ and U_0/δ_x, while those in the middle row amplify the hydrodynamic oscillation in the system. (For interpretation of the colors in the figure(s), the reader is referred to the web version of this article.)

$$\boldsymbol{F}(t_n) = -\sum_{\boldsymbol{\xi}_i,\, \boldsymbol{r}_j \in \mathbb{B}} \left[f_i(\boldsymbol{r}_j,\, t_n) + f_{\bar{i}}^{*}(\boldsymbol{r}_j + \delta_t \boldsymbol{\xi}_i,\, t_n) \right] \boldsymbol{\xi}_i, \quad \forall\, \boldsymbol{r}_j \in \Omega,\ \forall\, \delta_t \boldsymbol{\xi}_i + \boldsymbol{r}_j \notin \Omega, \tag{23}$$

where Ω denotes the flow domain and the set of boundary nodes $\mathbb{B}$ is defined in (21), $f_{\bar{i}}^{*}(\boldsymbol{r}_j + \delta_t \boldsymbol{\xi}_i,\, t_n)$ is the distribution function of $\boldsymbol{\xi}_{\bar{i}} := -\boldsymbol{\xi}_i$ bounced from the boundary and stored in the location $\boldsymbol{r}_j + \delta_t \boldsymbol{\xi}_i$ outside the fluid domain (or otherwise). When the boundary is located at the mid-point between two lattice nodes so the bounce-back scheme is exactly applicable, then $f_{\bar{i}}^{*}(\boldsymbol{r}_j + \delta_t \boldsymbol{\xi}_i,\, t_n) = f_i(\boldsymbol{r}_j,\, t_n)$. When boundary location is not located at the mid-point, $f_{\bar{i}}^{*}(\boldsymbol{r}_j + \delta_t \boldsymbol{\xi}_i,\, t_n)$ has to be reconstructed by, *e.g.*, interpolations [26].

The momentum exchange at the entire boundary is the total force $\boldsymbol{F}$ of (23) on the disc, which can be decomposed as the drag force $F_{\rm D}$, the lift force $F_{\rm L}$, and the force tangent to the disc boundary F_{θ}, all normalized by the Stokes drag force of the disc:

$$\bar{F}_{\rm D} = \frac{\sum_{\boldsymbol{r}_j \in \mathbb{B}} F_x(\boldsymbol{r}_j)}{6\pi\rho_0 \nu U_0 D}, \quad \bar{F}_{\rm L} = \frac{\sum_{\boldsymbol{r}_j \in \mathbb{B}} F_y(\boldsymbol{r}_j)}{6\pi\rho_0 \nu U_0 D}, \quad \bar{F}_{\rm t} = \frac{\sum_{\boldsymbol{r}_j \in \mathbb{B}} F_{\theta}(\boldsymbol{r}_j)}{6\pi\rho_0 \nu U_0 D}, \tag{24}$$

where $F_x(\boldsymbol{r}_j)$ and $F_y(\boldsymbol{r}_j)$ are the x and y components of the force on the disc near a boundary node $\boldsymbol{r}_j$, which is a fluid node near the boundary of the disc, and $F_{\theta}(\boldsymbol{r}_j)$ is the force tangent to the circumference near a boundary node $\boldsymbol{r}_j$. All the forces are computed from the momentum exchange at boundary nodes, given by (23).

To test the effectiveness of the proposed scheme for a moving body with rotational motion, we design the following set of simulations. Given a rotational rate ω_0 of the disc in a fixed reference frame at rest (mesh F), we choose several values of the rotation rates of mesh G, $\omega_{\rm G}$, and the disc, $\omega_{\rm C}$, such that $\omega_{\rm G} + \omega_{\rm C} = \omega_0$. In what follows, we fix $\omega_0 = 0.001/\delta_t$, and carry out four tests by varying both $\omega_{\rm G}$ and $\omega_{\rm C}$: (1) $\omega_{\rm G} = 0$ and $\omega_{\rm C} = \omega_0$, (2) $\omega_{\rm G} = \omega_0$ and $\omega_{\rm C} = 0$, (3) $\omega_{\rm G} = 0.002/\delta_t$ and $\omega_{\rm C} = -0.001/\delta_t$, and (4) $\omega_{\rm G} = 0.003/\delta_t$ and $\omega_{\rm C} = -0.002/\delta_t$.

We first simulate the flow with a Reynolds number Re = 30.0, *i.e.*, $s_\nu = 1.52$, $\nu = 0.0526\, c\delta_x$. In Case (1), mesh G does not rotate; it only moves horizontally according to the prescribed velocity $\boldsymbol{U}(t)$ given by (19). The velocity at the disc circumference is $\boldsymbol{\omega}_0 \times \boldsymbol{R} + \boldsymbol{U}(t)$, where $\boldsymbol{R}$ is the radial vector from the disc center to a point on its circumference. Since mesh G does not rotate in this case, there is no time dependent numerical artifact induced by the rotation of mesh G, thus it is used as the baseline solution for other cases to be benchmarked with.

The simulations are carried out for 16000 time steps. The evolution of the normalized drag force $\bar{F}_{\rm D}(t_n)$, the normalized lift force $\bar{F}_{\rm L}(t_n)$, and the normalized tangential force $\bar{F}_{\theta}(t_n)$ are shown for the Case (1) *vs.* Cases (2), (3), and (4) in Figs. 4. The following observations can be made. First of all, the variations of the forces shown in Fig. 4 exhibit three different underlying frequencies. The slowest variation is due to the hydrodynamic evolution of the initial conditions. This frequency is related to the Strouhal number in the system. The Reynolds number Re = 30.0 is in fact below the critical value beyond which the flow past a cylinder becomes unsteady. This variation is physical and is clearly seen in the inserts in the figures of the lift force $F_{\rm L}(t_n)$, which are shown in the middle row of Fig. 4.

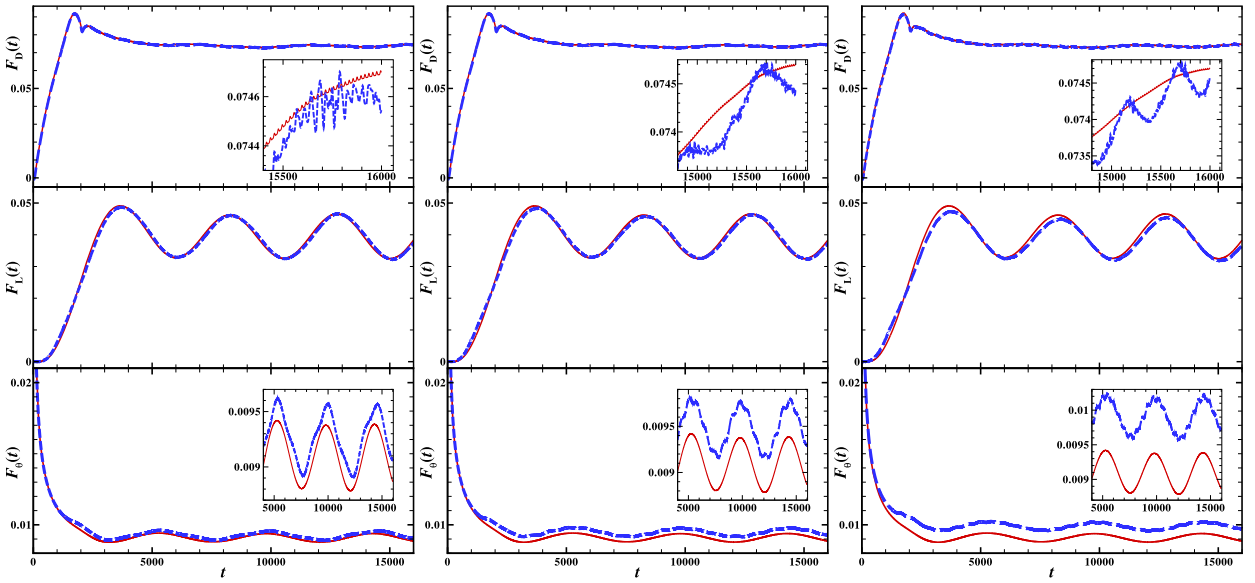

Fig. 5. Same as Fig. 4. Re = 60.0.

The other two faster frequencies manifest the numerical artifacts in the simulation. The slower frequency among the two is $2\omega_G/\pi$, which is generated by the rotation of mesh G. Because the mesh of the LBE is square and the zone on mesh G where the data communication between two meshes is circular, so the relative configuration of mesh G with respect to mesh F is invariant when mesh G rotates $\pi/2$ about its center, hence the frequency is $2\omega_G/\pi$. The oscillation with the frequency $2\omega_G/\pi$ can only be seen clearly from $\bar{F}_D(t)$ for Cases (3) and (4), as shown in the inserts of the top row of Fig. 4. From the inserts in the drag force $\bar{F}_D(t)$, on the top row of Fig. 4, it can be seen that the frequency due to the rotation of mesh G doubles as ω_G doubles. The fastest frequency is U_0/δ_x due to the linear motion of mesh G, and is the consequence of grid points in mesh F moving in and out of the zone in mesh G where the data communication between two meshes take place. This artifact has been magnified in the insert of Case (1), in the top figure of left column in Fig. 4. It should be stressed that the overset approach has drastically reduced the magnitude of this numerical artifact by several orders compared the previous approach without the overset [32]. As can be seen in Fig. 4, the magnitude of the numerical artifact due to the linear movement of mesh G is about $O(10^{-4})$ or less, compared to the magnitude of $\bar{F}_D(t)$ of $O(10^{-1})$. The magnitude of the numerical artifact due to the rotational movement of mesh G is about $O(10^{-3})$ or less.

We also simulate the flow with the Reynolds number Re = 60.0, *i.e.*, $s_v = 1.727$. The flow past a stationary cylinder becomes unsteady at the critical Reynolds number $\mathrm{Re}_c \approx 47.0$ (cf., *e.g.*, [54]) with the Strouhal number of *ca.* 0.135, corresponding to a period about $4700\delta_t$. At Re = 60.0, the flow past a rotating cylinder is expected to be unsteady.

In the lift force $F_L(t_n)$ shown in the middle row of Fig. 5, one can clearly see the slowest variation due to the unsteadiness of the flow, *i.e.*, the frequency of the von Kármán vortex street behind the cylinder determined by the Strouhal number of the system. We note that the magnitudes of the numerical artifacts due to both linear and rotational motions of mesh G remain the same, as in the case of Re = 30.0, the differences between the final value of the tangential force $\bar{F}_\theta(t)$ for the cases with $\omega_G \neq 0$ and that for the baseline case with $\omega_G = 0$ have increased slightly.

To analyze the numerical artifact due to the rotation of mesh G, we define the mean and fluctuating part of the tangential force after the initial acceleration of the disc:

$$\delta\bar{F}_\theta(t) := \bar{F}_\theta(t) - \langle\bar{F}_\theta(t)\rangle_t, \quad \langle\bar{F}_\theta(t)\rangle_t := \frac{1}{T_2 - T_1}\int_{T_1}^{T_2} \bar{F}_\theta(t)\,\mathrm{d}t, \tag{25}$$

where $T_1 = 6000\delta_t$ and $T_2 = 2.5T_1 = 15000\delta_t$ have been used, and $T_2 - T_1$ is about two periods of the hydrodynamic oscillation determined by the Strouhal number, which is about 0.13 at this Reynolds number. We then compute the tangential force difference with respect to the case of irrotational mesh G, *i.e.*, the case with $\omega_G = 0$:

$$\Delta\bar{F}_\theta(t;\,\omega_G) := \delta\bar{F}_\theta(t;\,\omega_G) - \delta\bar{F}_\theta(t;\,0). \tag{26}$$

The results of $\Delta\bar{F}_\theta(t;\,\omega_G)$ for Cases (2), (3), and (4) with Re = 60.0 are shown in Fig. 6.

For Case (2) of $\omega_G = 0.001/\delta_t$ and Case (3) $\omega_G = 0.002/\delta_t$, the magnitude of the fluctuating component of the tangential force, $\Delta\bar{F}_\theta(t;\,\omega_G)$, is at the level of $O(10^{-4})$, thus this part of the artifact is negligible. For Case (4) of $\omega_G = 0.003/\delta_t$, the component with the frequency of $2\omega_G/\pi$ has the magnitude of $O(10^{-4})$. In Case (4), however, it also has the component

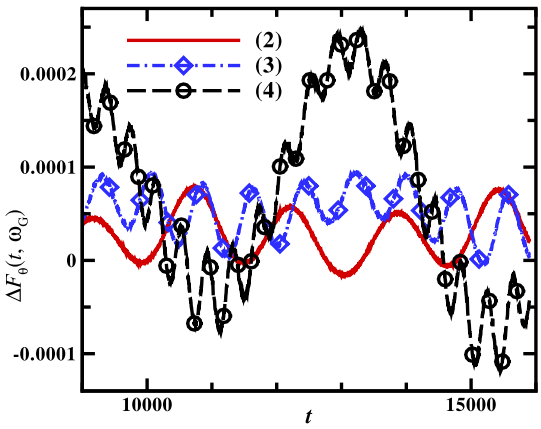

Fig. 6. The differences between the fluctuating tangential force with a non-zero ω_G and that with zero ω_G. Re = 60.0. Note that the magnitudes of the differences are of $O(10^{-4})$.

Table 1
The dependence of the mean tangential force $\langle \bar{F}_\theta(t; \omega_G)\rangle_t$ on ω_G, the angular velocity of mesh G. $\omega_G + \omega_C = \omega_0 = 0.001/\delta_t$. Re = 60.0.

ω_G	$\langle \bar{F}_\theta(t; \omega_G)\rangle_t$	$\langle \bar{F}_\theta(t; \omega_G)\rangle_t / \langle \bar{F}_\theta(t; 0)\rangle_t$
0.003	$9.468 \cdot 10^{-3}$	1.0881
0.002	$9.246 \cdot 10^{-3}$	1.0417
0.001	$9.094 \cdot 10^{-3}$	1.0169
0	$8.879 \cdot 10^{-3}$	1
−0.001	$8.879 \cdot 10^{-3}$	0.9764
−0.002	$8.462 \cdot 10^{-3}$	0.9309
−0.003	$7.721 \cdot 10^{-3}$	0.8496
−0.004	$6.518 \cdot 10^{-3}$	0.7170

with the hydrodynamic frequency determined by the Strouhal number of the system, as seen in Fig. 6. In all cases, the magnitude of the fluctuating component of the numerical artifact in the tangential force, $\Delta\bar{F}_\theta(t; \omega_G)$, is of the order $O(10^{-4})$, as opposed to the order of $O(10^{-1})$ in our previous work [32].

We next study the mean tangential force $\langle \bar{F}_\theta(t; \omega_G)\rangle_t$ and its dependence on the rotational velocity of mesh G, ω_G. The results of $\langle \bar{F}_\theta(t; \omega_G)\rangle_t$ and the ratio $\langle \bar{F}_\theta(t; \omega_G)\rangle_t / \langle \bar{F}_\theta(t; 0)\rangle_t$ are compiled in Table 1 for a number of values of ω_G. We note that the mean tangential force $\langle \bar{F}_\theta(t; \omega_G)\rangle_t$ varies significantly as ω_G varies, although it should not change in principle. However, the magnitude of the variation of the mean tangential force is of $O(10^{-4})$, therefore, this error does not affect the simulation much.

3.3. Flow fields

We now show the flow fields. Fig. 7 shows the contours of the normalized fluctuating pressure $\delta\bar{p}$ and the normalized vorticity $\bar{\omega}$ defined as the following:

$$\delta\bar{p}(x, y) := \frac{c_s^2\,\delta\rho(x, y)}{\rho_0 U_0^2/2}, \quad \bar{\omega}(x, y) := \frac{\omega(x, y)}{U_0/D}, \tag{27}$$

where $\delta\rho$ is the density fluctuation computed from the LB simulation, and $\omega := \partial_x u_y - \partial_y u_x$ is computed from the velocity field $\boldsymbol{u} = (u_x, u_y)$ with a finite difference. The results shown in Fig. 7 demonstrate that the flow fields computed with different values of ω_G are very close to each other, indicating that the numerical artifacts are indeed negligible.

We compute the L_2 differences of the velocity fields defined as the following:

$$\|\bar{\boldsymbol{u}} - \bar{\boldsymbol{u}}_*\|_p := \frac{\left[\sum_{\boldsymbol{r}_j \in \Omega'} \left|\boldsymbol{u}(\boldsymbol{r}_j) - \boldsymbol{u}_0(\boldsymbol{r}_j)\right|^p\right]^{1/p}}{\|\Omega'\|}, \quad p = 2, \tag{28}$$

where $\bar{\boldsymbol{u}}$ is the velocity field normalized by U_0, the reference velocity field $\bar{\boldsymbol{u}}_*$ is the one obtained with $\omega_G = 0$ and $\omega_C = 0.001$, *i.e.*, Case (1). Domain Ω' is a part of mesh F; its outer boundary is a rectangle of the size of 200×100, and its inner boundary is a circle of radius $R + 3\delta_x = 18.8\delta_x$ and concentric with the disc in the flow (cf. Fig. 3). Domain Ω' is chosen because most flow activities take place within it. Similarly, we also compute the L_2 differences of the normalized fluctuating pressure $\delta\bar{p}$ and vorticity $\bar{\omega}$, which are defined in Eqs. (27). The results are compiled in Table 2.

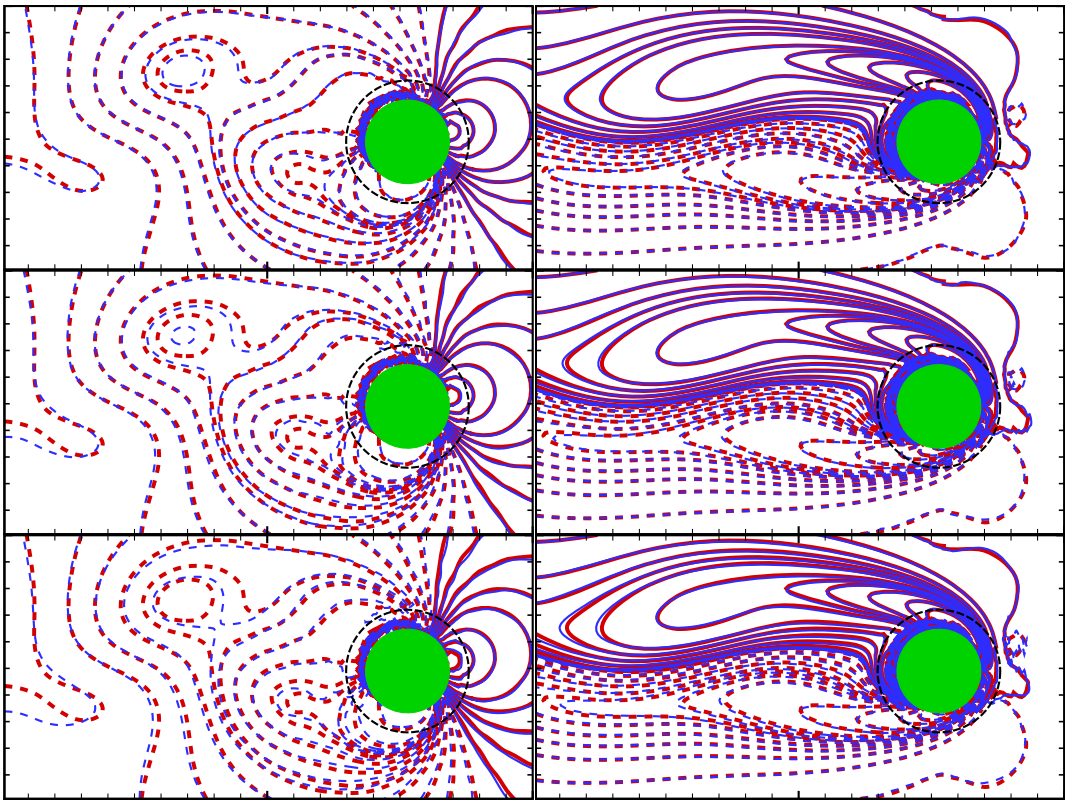

Fig. 7. Re = 60.0. The normalized pressure (left) and vorticity (right) at time $t_n = 8000\delta_t$. From top to bottom: Case (2), (3), and (4) (blue lines) *vs.* Case (1) (red lines). The dashed circle indicates the middle of the data-passing zone.

Table 2
The L_2 differences of the flow fields obtained at $t_n = 8000\delta_t$, with different values of ω_G and ω_C, $\omega_G + \omega_C = \omega_0 = 0.001$. Re = 60.0.

ω_G	-0.002	-0.001	0.001	0.002
ω_C	0.003	0.002	0.000	-0.001
$\|\bar{\boldsymbol{u}} - \bar{\boldsymbol{u}}_*\|_2$	$8.99 \cdot 10^{-3}$	$3.58 \cdot 10^{-3}$	$4.89 \cdot 10^{-3}$	$9.10 \cdot 10^{-3}$
$\|\delta\bar{p} - \delta\bar{p}_*\|_2$	$2.47 \cdot 10^{-4}$	$1.17 \cdot 10^{-4}$	$1.42 \cdot 10^{-4}$	$2.56 \cdot 10^{-4}$
$\|\bar{\omega} - \bar{\omega}_*\|_2$	$8.06 \cdot 10^{-2}$	$3.46 \cdot 10^{-2}$	$4.68 \cdot 10^{-2}$	$8.31 \cdot 10^{-2}$

It should be noted that the differences between the flow fields are due to the numerical artifacts of the rotating mesh. As can be seen from the data in Table 2, the differences grow with the angular velocity of the rotating mesh, ω_G. For $|\omega_G| \leq 0.002$, the differences in the velocity, the fluctuating pressure, and the vorticity due to the rotating mesh are of the order $O(10^{-3})$, $O(10^{-4})$, and $O(10^{-2})$, respectively.

4. Conclusion

In this work we propose to adopt the overset technique in the LBE for moving boundary problem in 2D. The objective is to reduce the noise generated by the relative motion of a moving body and the underlying Cartesian mesh. The transform of the moments between two meshes with relative rotation has been derived and all the forces due to rotational frame of reference have been considered. The proposed LB-overset scheme is validated with the flow of a disc moving in a rectangular domain with prescribed linear and rotational motion. The numerical results show that the numerical noise due to the motion of a rigid body relative to the underlying Eulerian mesh has been reduced by several orders of magnitude.

The proposed LB-overset scheme has only been applied to simulate the flow with one moving body in this work. However, it can be extended to include multiple moving bodies. For flows with multiple moving objects, adaptive mesh refinement has to be considered in order to simulate closing-up of moving bodies. This is to be our future research.

Declaration of competing interest

The authors declare that they have no known competing financial interests or personal relationships that could have appeared to influence the work reported in this paper.

Acknowledgements

The work is supported by The National Science Foundation of China (NSFC) through the Grants U1530401 and U1930402. The computational resources for the numerical simulations were provided by Beijing Computational Science Research Center (http://www.csrc.ac.cn).

References

[1] G.R. McNamara, G. Zanetti, Use of the lattice Boltzmann to simulate lattice-gas automata, Phys. Rev. Lett. 61 (1988) 2332–2335.
[2] F.J. Higuera, S. Succi, R. Benzi, Lattice gas dynamics with enhanced collisions, Europhys. Lett. 9 (4) (1989) 345–349.
[3] U. Frisch, Relation between the lattice Boltzmann-equation and the Navier-Stokes equations, Physica D 47 (1–2) (1991) 231–232, https://doi.org/10.1016/0167-2789(91)90293-I.
[4] A.J.C. Ladd, Numerical simulations of particulate suspensions via a discretized Boltzmann equation. Part 1. Theoretical foundation, J. Fluid Mech. 271 (1994) 285–309.
[5] A.J.C. Ladd, Numerical simulations of particulate suspensions via a discretized Boltzmann equation. Part 2. Numerical results, J. Fluid Mech. 271 (1994) 311–339.
[6] C.K. Aidun, Y. Lu, E. Ding, Direct analysis of particulate suspensions with inertia using the discrete Boltzmann equation, J. Fluid Mech. 373 (1998) 287–311, https://doi.org/10.1017/S0022112098002493.
[7] D. Qi, Lattice-Boltzmann simulations of particles in non-zero-Reynolds-number flows, J. Fluid Mech. 385 (1999) 41–62, https://doi.org/10.1017/S0022112099004401.
[8] A.J.C. Ladd, R. Verberg, Lattice-Boltzmann simulations of particle-fluid suspensions, J. Stat. Phys. 104 (5–6) (2001) 1191–1251.
[9] D. Qi, L.-S. Luo, Transitions in rotations of a nonspherical particle in a three-dimensional moderate Reynolds number Couette flow, Phys. Fluids 14 (12) (2002) 4440–4443.
[10] D. Qi, L.-S. Luo, Rotational and orientational behaviour of a three-dimensional spheroidal particles in Couette flow, J. Fluid Mech. 477 (2003) 201–213.
[11] H. Huang, X. Yang, M. Krafczyk, X.-Y. Lu, Rotation of spheroidal particles in Couette flows, J. Fluid Mech. 692 (2012) 369–394.
[12] H. Haddadi, J.F. Morris, Microstructure and rheology of finite inertia neutrally buoyant suspensions, J. Fluid Mech. 749 (2014) 431–459, https://doi.org/10.1017/jfm.2014.238.
[13] H. Haddadi, S. Shojaei-Zadeh, K. Connington, J.F. Morris, Suspension flow past a cylinder: particle interactions with recirculating wakes, J. Fluid Mech. 760 (2014) R2, https://doi.org/10.1017/jfm.2014.613.
[14] W. Mao, A. Alexeev, Motion of spheriod particles in shear flow with inertia, J. Fluid Mech. 749 (2014) 145–166, https://doi.org/10.1017/jfm.2014.224.
[15] Y. Sui, H.T. Low, Y.T. Chew, P. Roy, Tank-treading, swinging, and tumbling of liquid-filled elastic capsules in shear flow, Phys. Rev. E 77 (1,2) (2008) 016310, https://doi.org/10.1103/PhysRevE.77.016310.
[16] R.M. MacMeccan, J.R. Clausen, G.P. Neitzel, C.K. Aidun, Simulating deformable particle suspensions using a coupled lattice-Boltzmann and finite-element method, J. Fluid Mech. 618 (2009) 13–39, https://doi.org/10.1017/S0022112008004011.
[17] J. Gounley, Y. Peng, Shape recovery of elastic capsules from shear flow induced deformation, Commun. Comput. Phys. 16 (1) (2014) 56–74, https://doi.org/10.4208/cicp.220513.151113a.
[18] T. Krüger, B. Kaoui, J. Harting, Interplay of inertia and deformability on rheological properties of a suspension of capsules, J. Fluid Mech. 751 (2014) 725–745, https://doi.org/10.1017/jfm.2014.315.
[19] J. Gounley, Y. Peng, Computational modeling of membrane viscosity of red blood cells, Commun. Comput. Phys. 17 (4) (2015) 1073–1087, https://doi.org/10.4208/cicp.2014.m355.
[20] J. Tölke, M. Krafczyk, M. Schulz, E. Rank, Lattice Boltzmann simulations of binary fluid flow through porous media, Philos. Trans. R. Soc. Lond. Ser. A 360 (1792) (2002) 535–545.
[21] J. Tölke, S. Freudiger, M. Krafczyk, An adaptive scheme using hierarchical grids for lattice Boltzmann multi-phase flow simulations, Comput. Fluids 35 (8/9) (2006) 820–830.
[22] P. Lallemand, L.-S. Luo, Y. Peng, A lattice Boltzmann front-tracking method for interface dynamics with surface tension in two dimensions, J. Comput. Phys. 226 (2) (2007) 1367–1384.
[23] M. Geier, A. Fakhari, T. Lee, Conservative phase-field lattice Boltzmann model for interface tracking equation, Phys. Rev. E 91 (6), https://doi.org/10.1103/PhysRevE.91.063309.
[24] A. Fakhari, M. Geier, T. Lee, A mass-conserving lattice Boltzmann method with dynamic grid refinement for immiscible two-phase flows, J. Comput. Phys. 315 (2016) 434–457, https://doi.org/10.1016/j.jcp.2016.03.058.
[25] A. Fakhari, D. Bolster, L.-S. Luo, A weighted multiple-relaxation-time lattice Boltzmann method for multiphase flows and its application to partial coalescence cascades, J. Comput. Phys. 341 (2017) 22–43, https://doi.org/10.1016/j.jcp.2017.03.062.
[26] M. Bouzidi, M. Firdaouss, P. Lallemand, Momentum transfer of Boltzmann-lattice fluid with boundaries, Phys. Fluids 13 (11) (2001) 3452–3459.
[27] I. Ginzburg, F. Verhaeghe, D. d'Humières, Study of simple hydrodynamic solutions with the two-relaxation-times lattice Boltzmann scheme, Commun. Comput. Phys. 3 (3) (2008) 519–581.
[28] Z. Feng, E.E. Michaelides, The immersed boundary-lattice Boltzmann method for solving fluid-particles interaction problems, J. Comput. Phys. 195 (2) (2004) 602–628, https://doi.org/10.1016/j.jcp.2003.10.013.
[29] Y. Peng, L.-S. Luo, A comparative study of immersed-boundary and interpolated bounce-back methods in LBE, Prog. Comput. Fluid Dyn. 8 (1–4) (2008) 156–167.
[30] J.J. Quirk, An alternative to unstructured grids for computing gas-dynamic flows around arbitrarily complex 2-dimensional bodies, Comput. Fluids 23 (1) (1994) 125–142, https://doi.org/10.1016/0045-7930(94)90031-0.
[31] D. Calhoun, A Cartesian grid method for solving the two-dimensional streamfunction-vorticity equations in irregular regions, J. Comput. Phys. 176 (2) (2002) 231–275, https://doi.org/10.1006/jcph.2001.6970.
[32] P. Lallemand, L.-S. Luo, Lattice Boltzmann method for moving boundaries, J. Comput. Phys. 184 (2) (2003) 406–421.
[33] J.L. Steger, J.A. Benek, On the use of composite grid schemes in computational aerodynamics, Comput. Methods Appl. Mech. Eng. 64 (1–3) (1987) 301–326, https://doi.org/10.1016/0045-7825(87)90045-4.

[34] Z.J. Wang, V. Parthasarathy, A fully automated Chimera methodology for multiple moving body problems, Int. J. Numer. Methods Fluids 33 (7) (2000) 919, https://doi.org/10.1002/1097-0363(20000815)33:7<919::AID-FLD944>3.0.CO;2-G.
[35] Z.J. Wang, N. Hariharan, R.F. Chen, Recent development on the conservation property of Chimera, Int. J. Comput. Fluid Dyn. 15 (4) (2001) 265–278, https://doi.org/10.1080/10618560108970033.
[36] H.S. Tang, S.C. Jones, F. Sotiropoulos, An overset-grid method for 3D unsteady incompressible flows, J. Comput. Phys. 191 (2) (2003) 567–600, https://doi.org/10.1016/S0021-9991(03)00331-0.
[37] Y. Li, An improved volumetric LBM boundary approach and its extension for sliding mesh simulation, Ph.D. thesis, Iowa State University, 2011.
[38] R. Zhang, C. Sun, Y. Li, R. Satti, R. Shock, J. Hoch, H. Chen, Lattice Boltzmann approach for local reference frames, Commun. Comput. Phys. 9 (5) (2011) 1193–1205, https://doi.org/10.4208/cicp.021109.111110s.
[39] E.K. Far, M. Geier, M. Krafczyk, Simulation of rotating objects in fluids with the cumulant lattice Boltzmann model on sliding meshes, Comput. Math. Appl. 79 (1) (2020) 3–16, https://doi.org/10.1016/j.camwa.2018.08.055.
[40] H. Chen, Volumetric formulation of the lattice Boltzmann method for fluid dynamics: Basic concept, Phys. Rev. E 58 (3) (1998) 3955–3963, https://doi.org/10.1103/PhysRevE.58.3955.
[41] P. Ahlrichs, B. Dünweg, Simulation of a single polymer chain in solution by combining lattice Boltzmann and molecular dynamics, J. Chem. Phys. 111 (17) (1999) 8225–8239.
[42] D.L. Koch, A.J.C. Ladd, Moderate Reynolds number flows through periodic and random arrays of aligned cylinders, J. Fluid Mech. 349 (1997) 31–66.
[43] N.-Q. Nguyen, A.J.C. Ladd, Lubrication corrections for lattice-Boltzmann simulations of particle suspensions, Phys. Rev. E 66 (4) (2002).
[44] D. Qi, L.-S. Luo, R. Aravamuthan, W. Strieder, Lateral migration and orientation of elliptical particles in Poiseuille flows, J. Stat. Phys. 107 (1/2) (2002) 102–120.
[45] A. ten Cate, J. Derksen, L. Portela, H. van den Akker, Fully resolved simulations of colliding monodisperse spheres in forced isotropic turbulence, J. Fluid Mech. 519 (2004) 233–271, https://doi.org/10.1017/s0022112004001326.
[46] M.A. van der Hoef, R. Beetstra, J.A.M. Kuipers, Lattice-Boltzmann simulations of low-Reynolds-number flow past mono- and bidisperse arrays of spheres: results for the permeability and drag force, J. Fluid Mech. 528 (2005) 233–254, https://doi.org/10.1017/S0022112004003295.
[47] D. d'Humières, Generalized lattice-Boltzmann equations, in: B.D. Shizgal, D.P. Weave (Eds.), Rarefied Gas Dynamics: Theory and Simulations, in: Prog. Astronaut. Aeronaut., vol. 159, AIAA, Washington, D.C., 1992, pp. 450–458.
[48] P. Lallemand, L.-S. Luo, Theory of the lattice Boltzmann method: Dispersion, dissipation, isotropy, Galilean invariance, and stability, Phys. Rev. E 61 (6) (2000) 6546–6562.
[49] D. d'Humières, I. Ginzburg, M. Krafczyk, P. Lallemand, L.-S. Luo, Multiple-relaxation-time lattice Boltzmann models in three-dimensions, Philos. Trans. R. Soc. Lond. Ser. A 360 (1792) (2002) 437–451.
[50] P.J. Dellar, Lattice Boltzmann algorithms without cubic defects in Galilean invariance on standard lattices, J. Comput. Phys. 259 (2014) 270–283, https://doi.org/10.1016/j.jcp.2013.11.021.
[51] I. Ginzburg, D. d'Humières, Multireflection boundary conditions for lattice Boltzmann models, Phys. Rev. E 68 (6) (2003) 066614.
[52] P.J. Dellar, An interpretation and derivation of the lattice Boltzmann method using Strang splitting, Comput. Math. Appl. 65 (2013) 129–141.
[53] R. Mei, D. Yu, W. Shyy, L.-S. Luo, Force evaluation in the lattice Boltzmann method involving curved geometry, Phys. Rev. E 65 (2002) 041203.
[54] U. Fey, M. Konig, H. Eckelmann, A new Strouhal-Reynolds-number relationship for the circular cylinder in the range $47 < \mathrm{Re} < 2 \times 10^5$, Phys. Fluids 10 (7) (1998) 1547–1549, https://doi.org/10.1063/1.869675.